An Analysis of Hertzian Contact and Inner Race Crack-Induced Vibrations in a Coupled Shaft-Bearing System

Gilbert Emmanuel Ophel
Department of Industrial Engineering, Operations Management and Mechanical Engineering, Vaal University of Technology, Vanderbijlpark, South Africa
212000969@edu.vut.ac.za (corresponding author)

Bernard Xavier Tchomeni
Department of Industrial Engineering, Operations Management and Mechanical Engineering, Vaal University of Technology, Vanderbijlpark, South Africa
bernardt@vut.ac.za

Alfayo Anyika Alugongo
Department of Industrial Engineering, Operations Management and Mechanical Engineering, Vaal University of Technology, Vanderbijlpark, South Africa
alfayoa@vut.ac.za

Desejo Filipeson Sozinando
Department of Industrial Engineering, Operations Management and Mechanical Engineering, Vaal University of Technology, Vanderbijlpark, South Africa
desejos@vut.ac.za

Received: 28 June 2025 | Revised: 23 July 2025 and 2 August 2025 | Accepted: 20 August 2025

 DOI: https://doi.org/10.48084/etasr.13019

ABSTRACT

A dynamic model of a coupled shaft-bearing system was developed to examine the vibrational behavior caused by Hertzian contact mechanics and localized defects on the inner race. The model integrates mechanical energy balance, nonlinear Hertzian contact stiffness, and the Lagrangian formalism, considering the radial loads, system damping, and geometric characteristics. Numerical simulations executed via the fourth-order Runge–Kutta method reveal distinct vibrational signatures between the healthy and cracked bearing conditions. Under healthy operating conditions, broadband spectral energy is observed without significant peaks, indicating a uniform vibration behavior. The introduction of an inner race crack generates amplitude modulation, increased vibration levels, and pronounced spectral peaks between 600 Hz and 800 Hz. These peaks are consistent with defect-passing frequencies and nonlinear impact phenomena. This study reveals that the local defects significantly impact the dynamic response by producing complex, nonstationary vibration patterns that can be detected through time-domain analysis and power spectral density estimation using the power spectrum of the Fast Fourier Transform (FFT) technique.

Keywords-shaft–bearing system; Hertzian contact; inner race crack; vibration analysis; power spectrum analysis

I. INTRODUCTION

The rolling elements of bearings are critical components in rotating machinery that support the radial and axial loads and reduce the friction during operation. Defects in the bearing elements that cause vibrations, compromise the structural integrity and operational stability, affecting the machine performance. Cracks are a typical failure mechanism that produce localized disruptions in contact dynamics, leading to nonlinear force interactions and complex vibration signatures. The Hertzian contact theory is a fundamental framework for analyzing the bearing contact mechanics, providing insights into the stress distribution, deformation, and stiffness. In the context of EN31 rolling contact bearings used in screw

compressors, the Hertzian contact stresses are estimated using a combination of Gauss quadrature and statistical analysis, revealing that the stress magnitude increases with load and decreases with speed [1]. In the railway industry, the Hertzian theory aids in the analysis of the axle box roller bearing failures, confirming its applicability through finite element modeling, which identifies maintenance and lubrication as critical factors in the bearing failure [2]. The theory is also used in the dynamic modeling of deep groove ball bearings to simulate complex behaviors under fault conditions. This shows that the constant Hertz contact stiffness can approximate real-world conditions with minimal error [3–5]. Traditional time-frequency analysis techniques, such as those using the short-time Fourier transform, often struggle with nonstationary signals and noise interference, which are common in industrial environments [6-8]. Integrating time-frequency transformation and data analysis improves the acquisition of transient data and the diagnosis of faults in rotating machinery [9]. In the ultrasonic testing of anisotropic media, frequency-domain methods—including FFT-based feature extraction—are essential for the imaging defects by transforming the wave propagation data into an equivalent isotropic form, which facilitates the defect localization in complex materials [10-12]. The direction in which a roller passes over a cracked raceway affects the Time-Varying Displacement (TVD) and Time-Varying Stiffness (TVS) vibrations, with certain modes resulting in higher accelerations. This provides a basis for early fault detection and diagnosis in bearings [13]. Regarding slewing bearings in wind turbines, the crack extension is influenced by external loads and design parameters. These factors can be optimized to slow the crack growth and extend the bearings' service life [14]. The dynamic stability of rotor-bearing systems is also affected by cracks, with breathing cracks causing more instability than open cracks, especially when adjacent, leading to a broader range of unstable operating speeds [15]. Furthermore, the interaction between nonlinear forces (e.g., oil film forces) and cracks in rotor systems can result in complex vibration behaviors, including significant increases in specific frequency components, which are critical for fault diagnosis [16]. Misalignment and localized defects in bearings further complicate the vibration response because they alter the excitation durations and impact the acceleration depending on the location of the defect and the direction of the misalignment [17]. In more complex systems, such as the Rotating Shaft-Disc-Blade (RSDB), the coupling of multiple vibration sources and structural parameters requires comprehensive monitoring to detect and evaluate the severity of the blade cracks [18]. Advanced modeling techniques, such as variational neural networks, improve the prediction of bearing remaining useful life by focusing on bearing-specific vibration data, enhancing the fault detection and maintenance planning [19]. Additionally, innovative modeling approaches that optimize the contact angles in ball bearings can improve the accuracy and efficiency of dynamic analyses, which are crucial for understanding the effect of cracks on the bearing fatigue life [20].

This study develops a dynamic model of a coupled shaft-bearing system that includes Hertzian contact mechanics and the effects of inner race cracks, aiming to quantify the influence of the localized defects on the system vibrations under radial loads. Numerical simulations were performed in order to analyze time-domain responses, and spectral analysis was used to identify the frequency components induced by defects, providing insights into the vibration patterns associated with normal and defective states, improving the diagnostic capabilities for rotating machinery systems.

II. MODEL OF COUPLED SHAFT-BEARING SYSTEM

A model of a fully coupled shaft-bearing system was identified and established theoretically based on the mechanical energy law, involving kinetic, potential, and Rayleigh dissipation of the vibrating system. The system was analyzed in terms of an unbalanced shaft-bearing system, with each generalized coordinate of the system being accounted for using the Lagrange formalism. A single open crack bearing and fluid film bearing lubricant were established, while energy principles and fracture mechanism formalism were introduced to the coupled shaft-bearing vibration to govern the equation of the system. The degree of freedom of the fully coupled shaft-bearing system was derived using Lagrange equation, enabling the calculation of the shaft flexibility in two-orthogonal lateral deflections and shaft-bearing rotation for the system's coordinates. The shaft is modeled as a uniform, continuous elastic element with distributed mass and stiffness properties. The model's flexibility is determined by lumped parameters, with torsional effects not taken into account. The rotor-bearing system is simplified through the usage of lumped mass and stiffness elements, thereby facilitating the operation of a reduced-order dynamic model that is capable of capturing the dominant vibration modes without necessitating full-scale analysis. Figure 1 presents the dynamic model of the bearing system in two dimensions, capturing the elastic and damping interactions between the components.

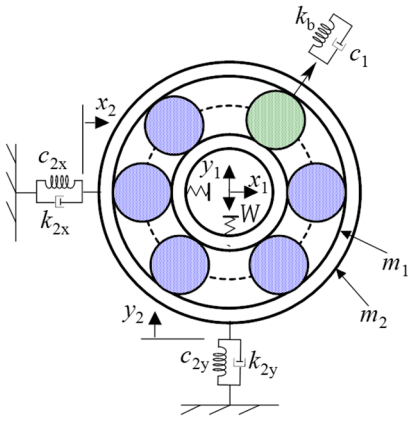

Fig. 1. Kinematic and structural layout of a ball bearing under radial load.

The inner race, mass m_1, and the outer race or housing, mass m_2, are connected through translational springs and dampers. The stiffness coefficients k_{1x}, k_{2x}, k_{1y}, and k_{2y} represent the directional stiffness properties of the bearing in the x and y axes. The damping terms c_1, c_{2x}, and c_{2y} are responsible for the energy dissipation resulting from lubricant film damping and material hysteresis. A nonlinear contact stiffness term, k_b, is included to model the Hertzian contact behavior between the

rolling elements and raceways. The displacement coordinates x_1, y_1 and x_2, y_2 represent the relative translational motion of the inner and outer masses, respectively, indicating how the system responds dynamically to radial loading and rotational excitation.

III. NONLINEAR HERTZIAN CONTACT FORCE

In mechanical systems that use rolling element bearings, the interaction between the rolling elements and the raceways is determined by non-linear contact mechanics. When a rolling element is subjected to an external force within a raceway, the local elastic deformation deviates from the linear equation of Hooke. Instead, the deformation is governed by the Hertzian contact theory, which describes the nonlinear elastic deformation that occurs at the contact interface between two curved surfaces under normal load. In the context of ball bearings, this contact gives rise to a nonlinear deformation force relationship, wherein the contact force is proportional to the deformation raised to a power greater than one. The center of the inner race displaces with respect to the outer race due to the application of radial forces, such as the weight of the rotor. The relative displacement between the races along the radial direction of a specific ball is determined by its instantaneous angular position, $\theta_i(t)$. If (x_1, x_2) and (y_1, y_2) represent the horizontal and vertical displacements of the inner and outer races, respectively, then the relative displacement between the races along the radial direction of a specific ball is determined by these two variables. The radial deflection δ_i experienced by ball i is described as the projection of this relative displacement onto the ball's radial direction, offset by the internal radial clearance C_r:

$$\delta_i = [(x_1 - x_2)\cos\theta_i + (y_1 - y_2)\sin(\theta_i) - C_r] \quad (1)$$

This expression is derived from the principle of deformation necessary to maintain contact between the ball and the races. In the case where $\delta_i > 0$, the ball undergoes compression, resulting in the generation of a restoring force in accordance with the nonlinear Hertzian contact law. If $\delta_i \leq 0$, it implies physical separation and that no contact force is transmitted at that instant. After establishing contact, the Hertzian contact theory, which describes the nonlinear elastic behavior of two curved surfaces under compression, can be expressed as [21]:

$$F_i = \begin{cases} K(\delta_i - \delta_d)^n if(\delta_i - \delta_d) > 0 \\ 0\ otherwise \end{cases} \quad (2)$$

The component of resolving the total restoring force along the x-axis and y-axis is:

$$F_x = \sum_{j=1}^{z} K(\delta_i - \delta_d)^n \cos(\theta_i) \quad (3)$$

$$F_y = \sum_{j=1}^{z} K(\delta_i - \delta_d)^n \sin(\theta_i) \quad (4)$$

where F_x and F_y are the components of restoring force in the x and y directions and z is the number of balls. In the present model, the contact stiffness for each rolling element is formulated using expressions derived from Hertzian theory, accounting for the geometric and material parameters [22]:

$$K = \frac{4(1-\nu^2)\rho g r^3}{E} \times \frac{2\pi G(1+4\beta^2)}{\kappa+1} \quad (5)$$

The dynamic behavior of the rolling elements is significantly influenced by the stiffness and damping characteristics at the contact interfaces between the rolling elements and the raceways.

IV. EQUATION GOVERNING THE MOTION OF THE SYSTEM

The development of a physically dynamic model for a rolling element bearing system is based on the principles of classical mechanics, particularly as they pertain to the Lagrange framework, resulting at a set of coupled, second-order differential equations of the system:

$$m_1\ddot{x}_1 + c_1\dot{x}_1 + k_{1x}(x_1 - x_2) = -F_x \quad (6)$$

$$m_1\ddot{y}_1 + c_1\dot{y}_1 + k_{1y}(y_1 - y_2) = -F_y - W_r \quad (7)$$

$$m_2\ddot{x}_2 + (c_1 + c_{2x})\dot{x}_1 + c_1\dot{x}_1 - k_{2x}x_2 = F_x \quad (8)$$

$$m_2\ddot{y}_2 + (c_1 + c_{2x})\dot{y}_1 + c_1\dot{y}_1 - k_{2y}y_2 = F_y \quad (9)$$

The equations describe the combined effects of inertial dynamics, linear elastic restoring forces, viscous energy dissipation, and nonlinear contact interactions. These interactions originate from the time-dependent engagement between the rolling elements and localized raceway defects. In the event of interaction between a rolling element and a defective surface region, the effective radial clearance and local compliance undergo modification. Such alterations result in a transient variation in the magnitude of the contact force, which can appear as amplitude modulation in the vibration signal. The severity and nature of the fault are typically influenced by three key geometric parameters: the angular position of the defect, its width, and its depth. The parameters in question influence the deformation's variation in relation to the ball's angular position, thereby determining the evolution of the restoring force over time. Figure 2 (a) presents the necessary geometry of the rolling element bearing, consisting of a set of spherical balls positioned between an inner and outer race. The inner and outer raceway diameters, d_i and d_o, respectively, provide the geometric context for analyzing the relative motion and spacing of the components. Figure 2 (b) shows the rolling element moving across a discrete defect on the inner race. Additionally, the ball enters the pre-contact phase during which it traverses the undisturbed section of the raceway. In this instance, the contact force remains constant, exhibiting no aberrant deflection. The trajectory of the ball is characterized by its smoothness and uniformity in its motion. As the ball progresses, it transitions to the direct contact phase during which it encounters the localized fault. The critical zone is distinguished by a sudden alteration in the surface continuity. The dimensions of the crack are determined by three parameters: its width W_d, depth D_d, and central angular position ϕ_d. At this point, an additional radial deflection d_r, is introduced due to the removal of material from the raceway. The contact force at the interface is either significantly reduced or momentarily interrupted, resulting in a sudden variation in the force transmission. Subsequent to the passage of the ball through the defect, the ball enters the post-contact phase, wherein it once again makes contact with the undamaged raceway surface. An additional radial deflection $\delta_d(\theta_i)$, is

introduced when the rolling element reaches the defective zone [23]:

$$\delta_d(\theta_i) = \begin{cases} d_d if\ mod & (\theta_i - \omega_c t + \phi_0, 2\pi) < \frac{\phi_d}{2} \\ 0\ otherwise & \end{cases} \quad (10)$$

where θ_i is the instantaneous angular position of the i-th ball, d_d is the defect depth, and ϕ_d is the angular width of the defect.

$$\phi_d(t) = \omega_c t + \phi_0 \quad (11)$$

where $\phi_d(t)$ is the time-varying angular position of the defect, ω_c is the shaft angular velocity, and ϕ_0 is the initial angular position of the defect. Each rolling element makes contact with the inner race at a location that is time-dependent. Consequently, the defect's interaction with the rolling element is determined by the relative motion between the rolling element and the moving defect region.

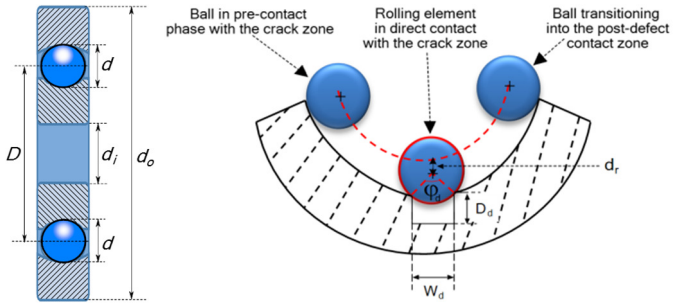

(a) (b)

Fig. 2. (a) Geometric definition of rolling element bearing components, (b) geometric and deflection parameters associated with an inner race localized defect.

V. NUMERICAL SIMULATION OF TIME DOMAIN RESPONSE OF THE SHAFT–BEARING SYSTEM

Time-domain waveforms are presented for different degrees of freedom, including lateral displacements of the rotor and outer race. Response values are derived through the numerical integration of the coupled nonlinear equations of motion, as established in the preceding sections. The numerical solution of the system is achieved through the integration of the fourth-order Runge–Kutta method. At each time increment, the angular positions of the balls and the defect are recalculated, the contact deflections are updated accordingly, and the resulting nonlinear forces are applied to update the displacement and velocity fields. The iterative process is continued over a simulation period that is sufficiently long to capture multiple shaft revolutions, thereby enabling the extraction of steady-state dynamic features. The response enables the visualization of vibration patterns, thus highlighting regions of dynamic amplification, periodicity disruption, and nonlinear damping effects. The bearing system is defined by specific geometric, mechanical, and defect parameters. The inner race diameter d_i, is 25 mm, while the outer race diameter d_o, is recorded at 52 mm. The pitch diameter, D, is measured at 39 mm, while the diameter of each ball is 8 mm, and the bearing contains $Z = 9$ balls. It can be deduced from the given data that the contact angle, α, is precisely 0 degrees, indicating that the load is purely radial. The rotor mass, m = 5.5 kg, contributes to the dynamic forces acting on the system. The defect is located on the inner race and has a depth D_d of 1 mm and a width W_d of 7 mm. The angular width of the distribution is 20°, and the initial angular position, θ_0, is 15°. Figure 3 (a) presents the waveform of a decaying oscillatory response, with an initial peak amplitude that approaches 0.001 m. The system demonstrates rapid oscillations within the initial 0.05 s, followed by a gradual decay in the amplitude, eventually stabilizing at approximately 0.005 m. Figure 3 (b) displays the vertical motion of the aforementioned rotor mass. The displacement amplitude is significantly lower, measuring approximately 10^{-3} m, hence emphasizing the damping properties in the vertical direction. In Figure 3 (c), the oscillatory response exhibits an initial peak near 10×10^{-3} m, which undergoes a gradual attenuation and stabilization around 5×10^{-3} m. The decay trend is characterized by a smooth and consistent decay, suggesting an effective energy dissipation through damping mechanisms. In Figure 3 (b), the vertical response shows a considerably diminished displacement scale, with a maximum amplitude of approximately 13×10^{-4} m and a minimum of 5×10^{-4} m. This observation indicates a reduction in the degree of compliance in the vertical direction of the outer race support, as evidenced by the low amplitude and rapid damping. The absence of modulation or nonlinear oscillatory behavior indicates that the system is operating in a nominal, fault-free condition.

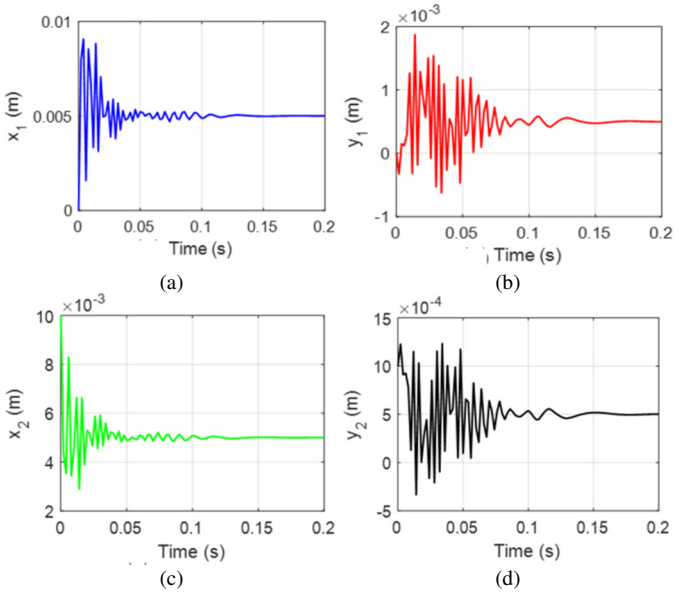

(a) (b) (c) (d)

Fig. 3. Healthy state response of rotor shaft center: (a) horizontal displacement of the inner race x_1, (b) vertical displacement of the inner race y_1, (c) horizontal displacement of the outer race x_2, (d) vertical displacement of the outer race y_2.

As depicted in Figure 4 (a), the response exhibits a marked deviation from the previously observed healthy-state waveform. The signal displays intermittent amplitude modulations and irregular fluctuations, accompanied by a substantial reduction in damping relative to the fault-free scenario. The amplitude oscillates between 0 m and 13×10^{-3} m, indicating periodic impact-like responses and loss of

dynamic symmetry due to the presence of the open crack. The vertical response in Figure 4 (b) further underscores the impact of the structural discontinuity. The waveform under examination demonstrates a sustained high-amplitude oscillation ranging between ±5 × 10^{-3} m, with pronounced amplitude modulation and possible beating phenomena. The signal exhibits an atypical decay pattern, indicative of a disruption in the dynamic equilibrium that characterizes a healthy state. This deviation leads to the appearance of secondary amplitudes, which are induced by the defect. As illustrated in Figure 4 (c), the horizontal displacement manifests a decaying oscillatory behavior that is discernibly different from the fault-free state. While initial transients comprise the initial portion of the waveform, the mid-to-late signal reveals irregular amplitude bursts and asymmetric oscillations around a mean level of approximately 0.005 m. The vertical response behavior exhibited in Figure 4 (d) demonstrates a distinctly modulated waveform, with amplitudes reaching up to 4 × 10^{-3} m. In comparison to the healthy condition, the signal demonstrates significantly elevated vibration levels and enhanced modulation depth [24]. The observed quasi-periodic vibration patterns, characterized by amplitude modulation and beating phenomena, are consistent with the trends reported in [25], where it was demonstrated that defect-induced excitations in the bearings generate complex time–frequency features, detectable through vibration and acoustic signal analysis. Authors in [26] corroborated the notion that such nonlinear dynamic responses, characterized by pronounced spectral peaks and harmonic sidebands, serve as indicators of defect-passing frequencies, even in the presence of high-noise conditions.

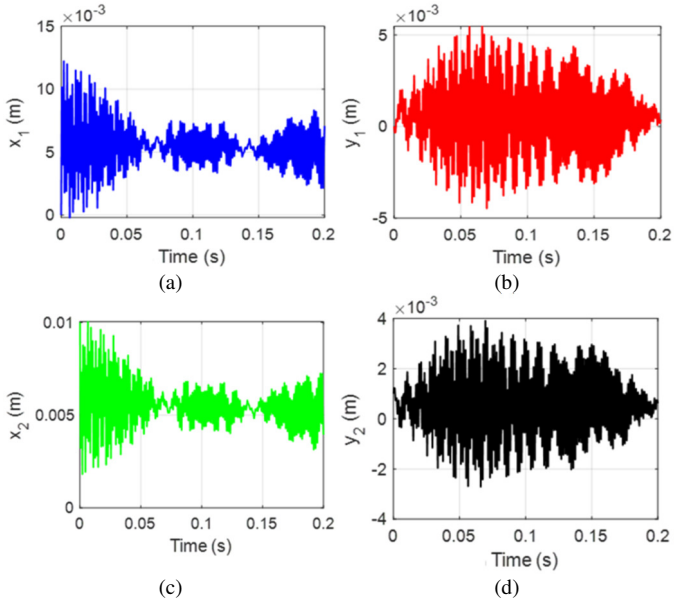

Fig. 4. Cracked state response of rotor shaft center: (a) horizontal displacement of the inner race x_1, (b) vertical displacement of the inner race y_1, (c) horizontal displacement of the outer race x_2, (d) vertical displacement of the outer race y_2.

VI. SIGNAL PROCESSING ANALYSIS OF THE SHAFT–BEARING SYSTEM

The dynamic behavior of a shaft-bearing system subjected to operational and fault-induced excitations is often characterized by complex, nonstationary, and multicomponent signals. To effectively evaluate and interpret these signals, advanced signal processing techniques are employed. The FFT is an efficient algorithm for computing the Discrete Fourier Transform (DFT) of a time-domain signal. The mathematical principle is the transformation of a discrete-time signal into its constituent frequency components. The FFT method is employed in the initial stage to transform the time-domain vibration response into the frequency domain. This process enables the identification of dominant harmonic components. Given a discrete-time signal $x[n]$ of length N, where n = 0,1, 2,…, N − 1, and the DFT is applied. The transforms the signal from the time domain to the frequency domain is [24]:

$$X[k] = \sum_{n=0}^{N-1} x[n] e^{-j\frac{2\pi}{N}kn}, k = 0,1,2,\ldots,N-1 \quad (12)$$

$$x[n] = \frac{1}{N}\sum_{k=0}^{N-1} X[k] e^{j\frac{2\pi}{N}kn}, n = 0,1,2,\ldots,N-1 \quad (13)$$

The FFT recursively divides a DFT of size N into smaller DFTs of size N/2, leveraging the divide-and-conquer strategy. The mathematical model remains unchanged; the focus is exclusively on enhancing the computational process. Figure 5 presents the power spectrum of x_1, which exhibits a broadband energy distribution primarily in the range between 100 Hz and 250 Hz. The absence of sharp peaks indicates that the system is not influenced by periodic excitations. The x_2 response closely mirrors the profile of x_1, with broadband energy predominantly between 100 Hz and 230 Hz. The absence of discrete spikes serves to reinforce the healthy state of the bearing, therefore indicating that the horizontal vibration transmission between the shaft and bearing housing occurs without impulsive content. A close examination of the power spectrum of y_2 reveals striking parallels with the y_1 response, particularly with regard to its high-energy content, which is centered around 230 Hz.

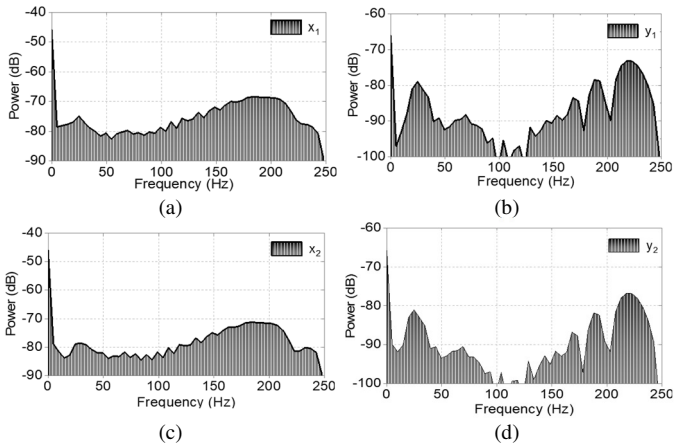

Fig. 5. Power spectrum of healthy state bearing system: (a) x_1, (b) y_1, (c) x_2, (d) y_2.

As shown in Figure 6, the x_1 spectrum exhibits distinct high-energy components emerging between 600 Hz and 800 Hz, with multiple sharp peaks indicative of the periodic impulses introduced by the crack. Lower-frequency components near 50 Hz, 200 Hz, and 300 Hz are also observable and may correspond to rotational harmonics and defect-passing frequencies. The vertical y_1 response of the shaft also exhibits a substantial deviation from the healthy condition. A high-intensity energy cluster is evident between 650 Hz and 800 Hz, with a clear peak around 740 Hz, reflecting elevated vibratory activity due to the defect. The x_2 response shows characteristics similar to the x_1 spectrum, with clear amplitude elevation and concentrated spectral energy between 650 Hz and 800 Hz. The recurrence of spectral spikes across mid and high frequencies indicates the transmission of fault-induced excitations from the shaft to the housing structure. The y_2 spectrum is indicative of a pattern of fault detection, with strong power concentration observed near 740 Hz and evident harmonic features below 300 Hz. These features may correspond to the Ball-Pass Frequency of the Inner race (BPFI) and its sidebands.

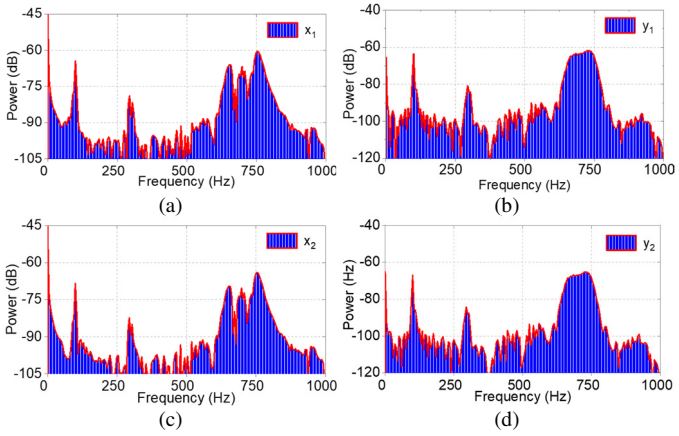

Fig. 6. Power spectrum of cracked state bearing system: (a) x_1, (b) y_1, (c) x_2, (d) y_2.

VII. CONCLUSIONS

The current study analyzed a dynamic model of a coupled shaft–bearing system, incorporating the presence of a localized defect crack on the inner race. The formulation integrates mechanics principles with nonlinear Hertzian contact theory to capture the complex interactions between the rolling elements and raceway surfaces under both healthy and defective states. The numerical simulations of the time-domain response demonstrated that an inner race defect introduces significant variations in the system's vibrational behavior. Such variations appear as amplitude modulations, increased vibration levels, and irregular oscillatory patterns. The former contrast sharply with the stable responses observed in the fault-free state. Further insights, as evidenced by the power spectral density plots, indicate that in the healthy bearing condition, the system manifests broadband frequency distributions without pronounced spectral peaks. This finding suggests uniform energy distribution and the absence of defect-induced periodic impulses. Conversely, the cracked bearing condition has exhibited discernible high-energy components and sharp spectral peaks. Furthermore, harmonics and sidebands are indicative of defect passing frequencies, and the presence of modulated vibration components is a consequence of defect interaction. Subsequent research could concentrate on extending the model to encompass variable load conditions and thermal influences, in addition to applying advanced signal processing techniques to enhance the defect detection and fault classification.

ACKNOWLEDGMENT

The authors express their sincere gratitude to the Vaal University of Technology, Department of Industrial Engineering, Operations Management and Mechanical Engineering, for providing support for the successful completion of this research.

NOMENCLATURE

Symbol	Description
α	Contact angle (degrees)
β	Geometric factor in Hertzian contact
Cr	Internal radial clearance (m)
c_1, c_{2x}, c_{2y}	Damping coefficients (N·s/m)
D_d	Depth of localized defect (m)
D	Pitch diameter of bearing (m)
d_i, d_o	Inner and outer raceway diameters (m)
d	Diameter of rolling element (m)
d_r	Defect radial deflection (m)
E	Young's modulus (Pa)
F_x, F_y	External force in x and y directions (N)
k_b	Hertzian contact stiffness (N/m)
k_{1x}, k_{1y}, k_{2x}, k_{2y}	Stiffness coefficients of bearing along x and y axes (N/m)
m_1, m_2	Mass of inner and outer race (kg)
N	Length of discrete signal for FFT
ρ	Material density (kg/m³)
t	Time (s)
W_d	Width of localized defect (m)
W	Radial load (N)
x_1, y_1	Inner race deflection along x and y axes (m)
x_2, y_2	Outer race deflection along x and y axes (m)
$X[k]$, $x[n]$	Discrete frequency and time-domain signal
Z	Number of balls in the bearing
θ_i	Instantaneous angular position (rad)
ϕ_d	Angular position of the defect (rad)
ω_c	Angular velocity of the shaft (rad/s)
ν	Poisson's ratio
δ_i	Radial deflection of the i-th ball (m)

REFERENCES

[1] S. H. Gawande, K. Balashowry, K. A. Raykar, and K. H. Munde, "Estimation of contact stresses in EN31 rolling contact bearings for screw compressor using Gauss quadrature & statistical analysis," *Australian Journal of Mechanical Engineering*, vol. 22, no. 5, pp. 894–910, 2023, https://doi.org/10.1080/14484846.2023.2195098.

[2] D. Javanmardi and M. A. Rezvani, "Rail vehicle axlebox roller bearing life and failure analysis based on the Hertz contact theory, finite element modeling, and field observations," *World Journal of Engineering*, vol. 21, no. 6, pp. 1183–1192, Nov. 2023, https://doi.org/10.1108/WJE-01-2023-0010.

[3] J. Shi *et al.*, "Three-Dimensional Dynamic Modeling and Vibration Analysis of Deep Groove Ball Bearings Under Compound Fault Excitation," Social Science Research Network, Rochester, NY, Jan. 18, 2025, https://doi.org/10.2139/ssrn.5102377.

[4] J. Hu, J. Shi, Y. Yu, W. Huang, C. Shen, and Z. Zhu, "Three-Dimensional Dynamic Analytical Modeling of Deep Groove Ball

Bearings with Fault Excitation," in *2023 International Conference on Sensing, Measurement & Data Analytics in the era of Artificial Intelligence (ICSMD)*, Xi'an, China, Aug. 2023, pp. 1–6, https://doi.org/10.1109/ICSMD60522.2023.10490904.

[5] J. Li, Y. Qi, P. Wu, J. Ding, and H. Ding, "Research on wear and grinding models of high-speed turnouts based on semi-Hertz contact," *Scientific Reports*, vol. 15, no. 1, Jan. 2025, Art. no. 531, https://doi.org/10.1038/s41598-024-85016-5.

[6] Y. Bella, A. Oulmane, and M. Mostefai, "Industrial Bearing Fault Detection Using Time-Frequency Analysis," *Engineering, Technology & Applied Science Research*, vol. 8, no. 4, pp. 3294–3299, Aug. 2018, https://doi.org/10.48084/etasr.2135.

[7] H. Jia *et al.*, "Short-time variational mode decomposition," *Signal Processing*, vol. 238, Jan. 2026, Art. no. 110203, https://doi.org/10.1016/j.sigpro.2025.110203..

[8] M. Al-Sa'd, T. Jalonen, S. Kiranyaz, and M. Gabbouj, "Quadratic Time-Frequency Analysis of Vibration Signals for Diagnosing Bearing Faults." arXiv, Feb. 08, 2024, https://doi.org/10.48550/arXiv.2401.01172.

[9] C. Zeng, "Frequency-domain defect imaging in anisotropic media based on coordinate transformation," *Physical Review Applied*, vol. 23, no. 1, 2025, Art. no. 014034, https://doi.org/10.1103/PhysRevApplied.23.014034.

[10] R. Suwondo, I. Hidayat, M. Suangga, M. Keintjem, and J. Walewangko, "Dynamic Assessment of a Railway Bridge using Operational Modal Analysis and Fast Fourier Transform: A Comparative Study with Finite Element Analysis," *Engineering, Technology & Applied Science Research*, vol. 15, no. 1, pp. 19200–19206, Feb. 2025, https://doi.org/10.48084/etasr.9202.

[11] A. F. Khalil and S. Rostam, "Machine Learning-based Predictive Maintenance for Fault Detection in Rotating Machinery: A Case Study," *Engineering, Technology & Applied Science Research*, vol. 14, no. 2, pp. 13181–13189, Apr. 2024, https://doi.org/10.48084/etasr.6813.

[12] B. X. Tchomeni Kouejou, D. F. Sozinando, and A. Anyika Alugongo, "Modeling and Analysis of Drill String–Casing Collision under the Influence of Inviscid Fluid Forces," *Applied Sciences*, vol. 13, no. 6, Jan. 2023, Art. no. 3557, https://doi.org/10.3390/app13063557.

[13] Z. Shi, G. Zhang, J. Liu, X. Li, Y. Xu, and C. Yan, "Influences of inclined crack defects on vibration characteristics of cylindrical roller bearings," *Mechanical Systems and Signal Processing*, vol. 207, Jan. 2024, Art. no. 110945, https://doi.org/10.1016/j.ymssp.2023.110945.

[14] S. Wang, J. Du, C. Li, S. Xia, S. Jiang, and J. Sun, "Crack propagation analysis of slewing bearings in wind turbines applying a modified sub-model technology," *Engineering Failure Analysis*, vol. 153, Nov. 2023, Art. no. 107556, https://doi.org/10.1016/j.engfailanal.2023.107556.

[15] C. Zhou, Y. Liu, W. Teng, H. Zhang, H. He, and C. Zhou, "Dynamic Modeling and Stability Analysis of a Heavy-Duty Flywheel Rotor-Bearing System with Two Cracks," *International Journal of Structural Stability and Dynamics*, vol. 22, no. 09, July 2022, Art. no. 2250103, https://doi.org/10.1142/S0219455422501036.

[16] Q. Ding, Z. Feng, Y. Zhang, and W. Sun, "Dynamic analysis of slant cracked rotor system considering nonlinear oil film force," *Plos One*, vol. 19, no. 1, 2024, Art. no. e0294293, https://doi.org/10.1371/journal.pone.0294293.

[17] Z. Wang, G. Li, X. Zhou, H. Zhang, Z. Lin, and S. Jia, "Dynamic analysis of deep groove ball bearing with localized defects and misalignment," *Journal of Sound and Vibration*, vol. 568, Jan. 2024, Art. no. 118071, https://doi.org/10.1016/j.jsv.2023.118071.

[18] L.-H. Yang, Y. Sun, Z.-B. Yang, Z. Mao, and X.-F. Chen, "Coupling vibration mechanism of rotating shaft–disc–blade system with blade crack—A systematical investigation on the effect of crack, condition, and structure parameters," *Thin-Walled Structures*, vol. 205, Dec. 2024, Art. no. 112398, https://doi.org/10.1016/j.tws.2024.112398.

[19] H. Wen, L. Zhang, and J. K. Sinha, "From Envelope Spectra to Bearing Remaining Useful Life: An Intelligent Vibration-Based Prediction Model with Quantified Uncertainty," *Sensors*, vol. 24, no. 22, Jan. 2024, Art. no. 7257, https://doi.org/10.3390/s24227257.

[20] D. Ruan, C. Gühmann, and J. Yan, "A new solving method for ball bearing dynamics model based on optimization with nonlinear constraints: Contact angles as iterative variables," *Journal of Manufacturing Processes*, vol. 106, pp. 338–346, Nov. 2023, https://doi.org/10.1016/j.jmapro.2023.09.076.

[21] Y. Yang, X. Qi, Y. Wang, M. Wang, B. Wen, and J. Zhai, "Dynamic Characteristics of a Cylindrical Roller Bearing with Cage Cracks," *Lubricants*, vol. 13, no. 1, Jan. 2025, Art. no. 25, https://doi.org/10.3390/lubricants13010025.

[22] P. Dong, Z. Gao, D. Xu, and S. Nyassi, "Rolling stiffness of contact surfaces during the rolling process of elastic particles," *Powder Technology*, vol. 445, Sept. 2024, Art. no. 120077, https://doi.org/10.1016/j.powtec.2024.120077.

[23] P. H. Jain, S. P. Bhosle, A. J. Keche, and R. G. Desavale, "A Dynamic Model of Outer Race Defective Bearing Considering the Unbalanced Shaft-Bearing System With Experimental Simulation," *Journal of Tribology*, vol. 146, no. 1, Oct. 2023, Art. no. 014301, https://doi.org/10.1115/1.4062689.

[24] M. Wang, X. Fu, X. Yan, and L. Teng, "A New Chaos-Based Image Encryption Algorithm Based on Discrete Fourier Transform and Improved Joseph Traversal," *Mathematics*, vol. 12, no. 5, Jan. 2024, Art. no. 638, https://doi.org/10.3390/math12050638.

[25] . M. Iqbal, A. K. Madan, and N. Ahmad, "Vibration and acoustic signal-based bearing fault diagnosis in CNC machine using an improved deep learning," *Iran Journal of Computer Science*, vol. 7, no. 4, pp. 723–733, Dec. 2024, https://doi.org/10.1007/s42044-024-00205-9.

[26] R. Wang, S. Zhang, S. Liu, W. Liu, and A. Ding, "A bearing fault diagnosis method for high-noise and unbalanced dataset," *Smart and Resilient Transportation*, vol. 5, no. 1, pp. 28–45, Dec. 2022, https://doi.org/10.1108/SRT-04-2022-0005.